

# *Ab initio* study of the electronic, mechanical, and vibrational properties of different $\text{Al}_2\text{Si}_2\text{Sr}$ crystalline phases

A. M. Garay-Tapia, Gerardo Trapaga, and Aldo H. Romero  
 CINVESTAV-Unidad Querétaro, Libramiento Norponiente 2000, CP 76230, Querétaro, México

Raymundo Arróyave

Department of Mechanical Engineering and Materials Science and Engineering Program, Texas A&M University, ENPH 119,  
 Mail Stop 3123, College Station, Texas 77843-3123, USA

(Received 9 November 2010; revised manuscript received 24 February 2011; published 30 June 2011)

We report a series of density functional calculations for different crystalline structures in the alloy  $\text{Al}_n\text{Si}_m\text{Sr}$  family. We perform a complete characterization for different crystalline space groups of the  $\text{Al}_{0.4}\text{Si}_{0.4}\text{Sr}_{0.2}$  alloy by determining the electronic structure and the mechanical and vibrational properties. In particular, we report on studies of Pnma, Cmcn, tI10, and  $\overline{P}3m1$  unit cells based as crystalline structures, as they have been proposed in studies of similar alloys. The calculations show a large diversity of properties, depending on the basic crystalline structure. We determine their elastic properties, energetics, and vibrational stability.

DOI: [10.1103/PhysRevB.83.214111](https://doi.org/10.1103/PhysRevB.83.214111)

PACS number(s): 64.60.-i, 71.15.Mb, 63.20.D-

## I. INTRODUCTION

$\text{Al}_2\text{Si}_2\text{Sr}$  is a very important technological compound in the industry of light metal casting. In particular, it has been noted that the tuning of different external parameters can largely modify the growth mechanism of this compound, which has important implications in the mechanical and structural properties of aluminum-silicon eutectic alloys. Basically, the addition of Sr in the aluminum-silicon alloy modifies, to a large extent, the structural properties and therefore produces important changes in many of the physical properties of the original alloy, such as tensile, impact, fatigue, and machinability.<sup>1</sup> According to the ternary phase diagram,<sup>2</sup> the ternary eutectic monovariant line lies very close to the binary eutectic. Therefore, small amounts of strontium are sufficient to produce changes in the microstructure of Al-Si alloys and largely modify the morphology of silicon crystallites.<sup>3</sup> However, the addition of Sr can cause microstructural changes, from acicular to fibrous silicon, which in turn modify mainly the machinability (and manufacturing) properties of these alloys. The addition of Sr also promotes the formation of the  $\text{Al}_2\text{Si}_2\text{Sr}$  phase, modifying the mechanical properties and leading to a suppression of the strontium effects on silicon crystallites. For these reasons, knowledge of the properties and the stability of this phase becomes important to clarify issues which can have an impact on the properties and the modification process.

In regard to the different recognized properties for this ternary alloy, just recently it has been demonstrated that one of the synthesized phases corresponds to a *trigonal* ( $\overline{P}3m1$ ) crystal structure with thermoelectric properties, as shown by Kauzlarich.<sup>4</sup> Unfortunately, its thermoelectric figure of merit has been found to be too low for practical applications. However, clathrate-like phases have been found in general to be promising thermoelectric materials.<sup>5</sup> For example, in the Ba-Al-Si system, experiments have shown the appearance of this property in  $\text{Al}_2\text{Si}_2\text{Ba}$ , which has an orthorhombic space group (Pnma), where there are cages formed by just Al-Si surrounding Ba atoms in a clathratelike arrangement.<sup>5</sup> Recent investigations<sup>6,7</sup> have also shown that there is a structural phase transition between orthorhombic (Pnma) and tetragonal

(I4/mmm) unit cells at different conditions of pressure and temperature, which could indicate that there is a good possibility to be able to manipulate the appearance of the clathrate phase. Another possible phase, obtained for the  $\text{Al}_2\text{Si}_2\text{Ba}$  system, has been recently reported by Yamanaka.<sup>8</sup> In this particular case, the structure corresponds to an orthorhombic (Cmcn) unit cell, with Al-Si cages surrounding Ba atoms. Such synthesis has been obtained by applying high-pressure and high-temperature (HPHT) conditions. Given the fact that the  $\text{Al}_2\text{Si}_2\text{Sr}$  alloy is similar to other synthesized systems, it could be expected that those reported phases could also be present in the  $\text{Al}_2\text{Si}_2\text{Sr}$  alloy.

Although the synthesis and characterization of  $\text{AM}_2\text{X}_2$  compound [ $A$  = rare earth,  $M$  = (Al, Ga), and  $X$  = (Si, Ge)] alloys have been of interest for many years, the case of pure  $\text{Al}_2\text{Si}_2\text{Sr}$  has not been fully characterized. For example, the elastic constants, the formation free energy, and even the consideration of a structural phase transition in well-controlled environments have not been reported. Such knowledge is of vital importance in the industry of silicon casting alloys. In these types of compounds, it is widely accepted that they crystallize in tetragonal (I4/mmm) (Ref. 9) or hexagonal ( $\overline{P}3m1$ ) (Ref. 10) crystal structures, depending on the valence electrons.<sup>11,12</sup> As mentioned above, some reports suggest that these compounds can also crystallize as an orthorhombic phase.

In this work, we report a detailed analysis of the electronic structure and the mechanical and vibrational properties of the orthorhombic (both Pnma and Cmcn), tetragonal (I4/mmm), and trigonal ( $\overline{P}3m1$ ) phases with a  $\text{Al}_{0.4}\text{Si}_{0.4}\text{Sr}_{0.2}$  composition, with the goal of gaining an understanding of the structural behavior of the Al-Si alloy system when Sr is used as a modifier element. Besides the structural and electronic characterization, we will also discuss their potential application as thermoelectric materials.

The following section describes the theoretical approximations and the different parameters used in our calculations. Then we proceed to describe the theoretical results obtained by rationalizing our findings with different physical quantities.

We finish by discussing the meaning of our calculations as well as presenting some predictions based on our results.

## II. METHODOLOGY

### A. Ground-state properties

The electronic-structure calculations were performed within the density functional theory (DFT)<sup>13</sup> formalism as implemented within the Vienna *ab initio* simulation package (VASP).<sup>14,15</sup> We have considered three different approximations for the exchange-correlation functional: the local density approximation (LDA) according to the Perdew-Zunger parametrization,<sup>16</sup> and two different generalized gradient approximations, Perdew-Wang 1991 (GGA-PW91) (Ref. 17) and the most recent Armiento-Mattsson 2005 (GGA-AM05) (Refs. 18 and 19). This allows us to discriminate the dependence of our results with respect to the theoretical approximations used to describe the exchange correlation. Wave functions were expanded in plane waves, using only valence electrons described within the projector augmented-wave (PAW) pseudopotential method. The Brillouin-zone integrations were performed using a Monkhorst-Pack mesh.<sup>20</sup> Full relaxations were performed by using the Methfessel-Paxton smearing method of order one<sup>21</sup> and a final self-consistent static calculation with the tetrahedron smearing method with Blochl corrections.<sup>22</sup> An energy cutoff of 350 eV was used for all calculations and a  $k$ -point mesh of  $15 \times 15 \times 9$  and  $13 \times 13 \times 13$ , equivalent to 10,000  $k$ points/reciprocal atom, for the structures trigonal (P-3m1) and tetragonal (I4/mmm) was used. For the monoclinic (C2/m) and orthorhombic (Pnma) structures, a  $k$ -point mesh of  $10 \times 10 \times 5$  and  $5 \times 12 \times 5$ , equivalent to 5000  $k$  points/reciprocal atom, was used. With these parameters, a convergence in energy of 1 meV and 1 kbar in pressure was reached.

### B. The elastic-constant calculation

For the evaluation of the elastic constants, the ground state and fully relaxed structures were strained in different directions according to their symmetry. The total-energy changes were evaluated according to a Taylor expansion<sup>23</sup> for the total energy with respect to the applied strain in the following way:

$$E(V, \delta) = E_0 + V_0 \left[ \sum_i \tau_i \epsilon_i \delta_i + \frac{1}{2} \sum_{ij} C_{ij} \tau_j \epsilon_j \delta_j \right], \quad (1)$$

with the strain tensor given by

$$\epsilon = \begin{pmatrix} \epsilon_1 & \frac{1}{2}\epsilon_6 & \frac{1}{2}\epsilon_5 \\ \frac{1}{2}\epsilon_6 & \epsilon_2 & \frac{1}{2}\epsilon_4 \\ \frac{1}{2}\epsilon_5 & \frac{1}{2}\epsilon_4 & \epsilon_3 \end{pmatrix}. \quad (2)$$

The energy of the unstrained system is denoted as  $E_0$ . That is the energy at equilibrium volume  $V_0$ .  $C_{ij}$  corresponds to the elastic constant,  $\tau_i$  is an element in the stress tensor, and  $\epsilon_0$  is a factor which takes care of the Voigt index.<sup>24</sup> The strained energy was calculated within the LDA, GGA-PW91, and GGA-AM05 approximations using the same energy cutoff previously mentioned and conserving the density of the  $k$ -point mesh for the strained structures. This was intended to address

the dependence of the elastic properties with respect to the given approximations of the exchange correlation.

We calculate the elastic constants for a trigonal phase with different strains. Due to the fact that the energy expansion is only performed to second order, it is important to check if the strain value guarantees the harmonic behavior. For this purpose, we performed a convergence study for different strain values (0.02, 0.035, 0.05, 0.065, 0.085) and found that the value of 0.05 is sufficient to ensure good accuracy. Due to symmetry constraints, it was necessary to use different strain-value conditions for the trigonal ( $P\bar{3}m1$ ), tetragonal ( $I4/mmm$ ), and orthorhombic (both  $Cmcm$  and  $Pnma$ ) structures; strains and parametrization were used according to Ref. 25. The number of necessary elastic constants is reduced completely by crystalline symmetry.

### C. Thermodynamic and vibrational properties

The thermodynamic properties at finite temperatures can be calculated by considering the entropic contributions to the total free energy. In this case, the main considered entropic contribution was due to the vibrational degrees of freedom. The vibrational effects are only considered under the harmonic approximation.<sup>26</sup> This approach is based on a Taylor expansion of the crystal potential around the atomic equilibrium positions (also called the frozen phonon approximation). Using the supercell method,<sup>27</sup> we are able to calculate the interatomic force constants. The Fourier transform of this interatomic-force-constant matrix (the dynamical matrix) can be diagonalized, where its eigenvalues correspond to the structure-vibration normal eigenmodes (phonons) and its eigenvectors correspond to the atomic vibrations to that specific eigenfrequency. The vibrational free energy is obtained as a function of temperature<sup>26</sup> by using the phonon density of states (DOS), according to the following equation:

$$F_{\text{vib}}(T) = k_B T \int_0^\infty \ln \left[ 2 \sinh \left( \frac{h\nu}{2k_B T} \right) \right] g(\nu) \nu d\nu, \quad (3)$$

where  $g(\nu)$  corresponds to the phonon DOS and  $k_B$  is the Boltzmann constant. The vibrational properties were calculated in this work by interfacing the interatomic force constants obtained from VASP with the ATAT software package.<sup>28</sup> An atomic displacement of 0.05 Å was used in all phonon analyses discussed below. The number of independent displacements necessary to calculate the total-force-constant matrix was determined from the symmetry of the considered structure and as generated from the ATAT code.<sup>28</sup>

## III. RESULTS AND DISCUSSION

### A. Crystal structure and ground-state properties

The ground-state crystal structures for the four considered phases of the alloy  $\text{Al}_2\text{Si}_2\text{Sr}$  were optimized by using the crystallographic information of the prototype phases, which were previously studied in the  $\text{Al}_2\text{Si}_2\text{Ba}$  alloy. Table I shows the comparison of the optimized structural parameters and the prototype cell parameters, with the three considered exchange correlations. In the case of the trigonal ( $P\bar{3}m1$ ) phase, the structural values of the prototype structure happen to be quite close to the calculated ones and lie between the

TABLE I. Comparison of the optimized structural parameters and the prototype cell parameters, with the three considered exchange correlations. Crystallographic data for the  $\text{Al}_2\text{Si}_2\text{Si}$  phase has been taken from analogous systems reported in the literature.

Phase	Prototype	Space group	Cell parameters <sup>a</sup> (Å)	Calculated parameters (Å)		
				LDA	GGA-PW91	GGA-AM05
op20 <sup>d</sup>	$\text{Al}_2\text{Si}_2\text{Ba}^7$	Pnma 62	a = 10.073	9.751	9.973	9.860
			b = 4.225	4.105	4.171	4.129
			c = 10.865	10.618	10.777	10.717
os20 <sup>d</sup>	$\text{Al}_2\text{Si}_2\text{Ba}^8$	Cmcm 63	a = 4.238	4.218	4.272	4.253
			b = 10.890	10.252	10.469	10.371
			c = 10.106	10.173	10.359	10.235
tI10 <sup>c</sup>	$\text{Al}_2\text{Si}_2\text{Ba}^8$	I4/mmm 139	a = 4.231	4.131	4.178	4.225
			b = 4.231	4.131	4.178	4.225
			c = 12.601	11.349	12.011	11.015
Tri <sup>b</sup>	$\text{Al}_2\text{Si}_2\text{Sr}^{29}$	$\text{P}\bar{3}\text{m}1$ 164	a = 4.179	4.145	4.206	4.177
			b = 4.179	4.145	4.206	4.177
			c = 7.429	7.252	7.439	7.339

<sup>a</sup>Cell parameters of the prototype phases.

<sup>b</sup>Trigonal.

<sup>c</sup>Tetragonal.

<sup>d</sup>Orthorhombic.

exchange correlations. However, for the other crystal phases, the experimental values for the Ba alloys are much larger than the calculated Sr alloys. This is mainly due to the atomic size for the Ba case. To facilitate the identification of the different structures, we define the following notation: the orthorhombic (Pnma) structure is identified as op20, the orthorhombic (Cmcm) as os20, the tetragonal (I4/mmm) as tI10, and the trigonal ( $\text{P}\bar{3}\text{m}1$ ) as tri.

The optimized structures are depicted in Fig. 1. The left column in this figure corresponds to the unit cell and the center column shows the clathrate structure for op20 and os20. In the case of tI10 and tri, the center column shows the conventional unit cell. The right column shows the structures, where we have defined a tetrahedron around the aluminum atoms. It is found that most aluminum atoms are fourfold coordinated for the considered phases. While both op20 and os20 are clathrates with Al-Si cages, there is a noticeable difference with respect to the atomic coordination. For op20, there are four Si atoms on the tetrahedron corners, while in the os20 structure, there are three Si atoms plus one Al atom in the corners. This different Al-Al bond rearrangement has important implications for their properties. In particular, in the case of the os20, it happens to be less stable than op20.

This is in agreement with the general observation presented by Blake *et al.*<sup>30</sup> that the structural stability is reduced as a function of the presence of M-M metallic bonds, which usually is less strong. Therefore, the os20 structure happens to be less stable than the op20 structure, as seen in Table II, where the formation enthalpy is the smallest of all phases.

In the case of the tI10 and the tri phases, the Al-Si tetrahedrons are between strontium atoms. These two phases happen to be quite similar, with tetrahedrons in a tetrahedral arrangement and with angles close to  $109.5^\circ$ . The Sr-Sr bond distance is less in the tI10 phase, which makes it a more compact phase. The formation enthalpy is reported in Table II, which shows a small difference between the two

structures when the GGA-AM05 and LDA functionals are used, while it is much larger if GGA-PW91 is used. From the LDA and GGA-PW91 exchange correlations, the trigonal structure is found to be the lowest energy configuration, while in GGA-AM05, tI10 is the ground-state structure. Therefore, the trigonal tI10 and the metastable op20 phases can be stabilized by temperature and/or pressure.

## B. Electronic structure

After performing calculations using the considered exchange correlations, we did not find any significant difference. Therefore we only discuss the electronic-structure data obtained from the LDA exchange correlation functional. In Fig. 2, we show the electronic density of states. The four phases show metallic behavior; the trigonal and the op20 phases are those that have fewer states at the Fermi level, mainly because the electrons are more localized around the atoms and less into the molecular states, as discussed below.

The Al-Si-Sr phases correspond to Zintl-like phases.<sup>31</sup> In a Zintl compound, each constituent attains a closed valence shell by combining a formal charge transfer with covalent bonds: the more-electropositive atoms donate their valence electrons to the more-electronegative atoms, such that they can complete the octet rule. In the Al-Si-Sr phases, the Al and Sr atoms in the structure donate their valence electrons to Si in order to fulfill the Zintl concept. However, the four phases do not exactly follow this rule. A Bader charge analysis<sup>32</sup> was used to determine the charge transfer and to identify the bond type. In the case of the trigonal phases, the os20 and op20 phases, Fig. 2 shows how the electron conduction is produced mainly by the *p* electrons coming from all three different atoms, while the *s* and *d* orbitals are hybridized. The Bader maxima show, for the trigonal and op20 phases, that the electrons are localized between the Al-Si atoms, where Al is the donor. The Zintl concept can be reinforced by looking at

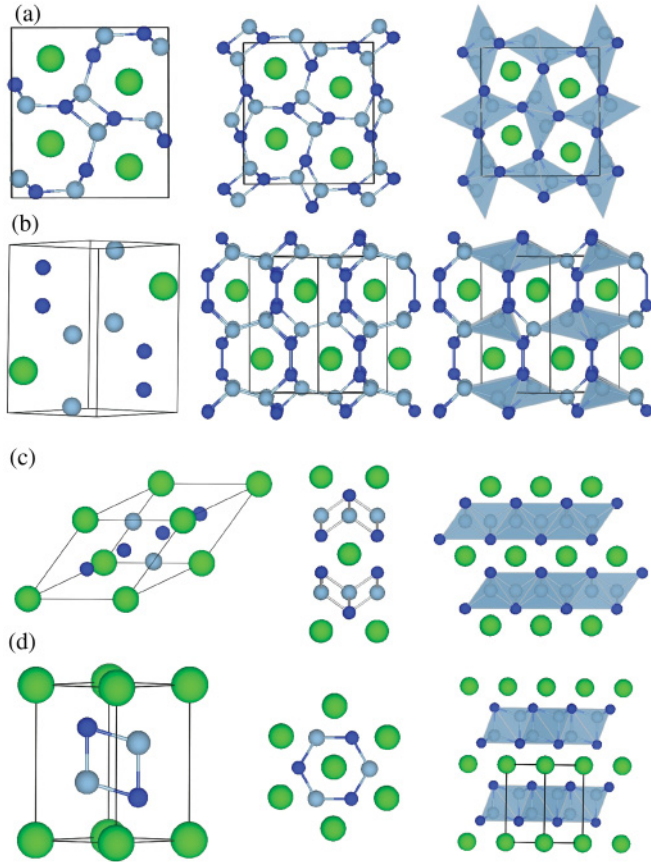


FIG. 1. (Color online) Crystal structures in the  $\text{Al}_{0.4}\text{Si}_{0.4}\text{Sr}_{0.2}$  composition (Al: medium gray circles, Si: small blue circles, Sr: large green circles). (a) op20, (b) os20, (c) tI10, and (d) tri. The first column shows the unit cell for all structures. For the op20 and os20 phases, the second column shows the clathrate structure where the Ba atoms are surrounded by the Al-Si atoms. For the tI10 and tri phases, the second column shows the conventional cell. The third column shows the tetrahedral representation around the fourfold coordinated aluminum.

the charge contribution of Sr to Si. Basically, the aluminum atom donates its three valence electrons to silicon where they are forming a fourfold coordinated structure. This structure is anionic and the Sr atoms promote their electrons as a cation.

The case for the tI10 phase is different than the previously described structures. Figure 2 shows again that the conduction is on the  $p$  electrons. However, there is a high contribution coming from the  $s$  and  $p$  orbitals, where the hybridization is

TABLE II. Formation enthalpy calculated by first principles [kJ/(mol atom)].<sup>a</sup>

Phase	Space group	LDA	GGA-PW91	GGA-AM05
op20	Pnma	-28.930	-28.442	-22.960
os20	Cmcm	-22.345	-22.352	-16.147
tI10	I4/mmm	-29.485	-25.754	-25.222
Tri	P $\bar{3}$ m1	-31.384	-31.005	-25.180

<sup>a</sup>Reference states: fcc for Sr and Al, diamond cubic for Si.

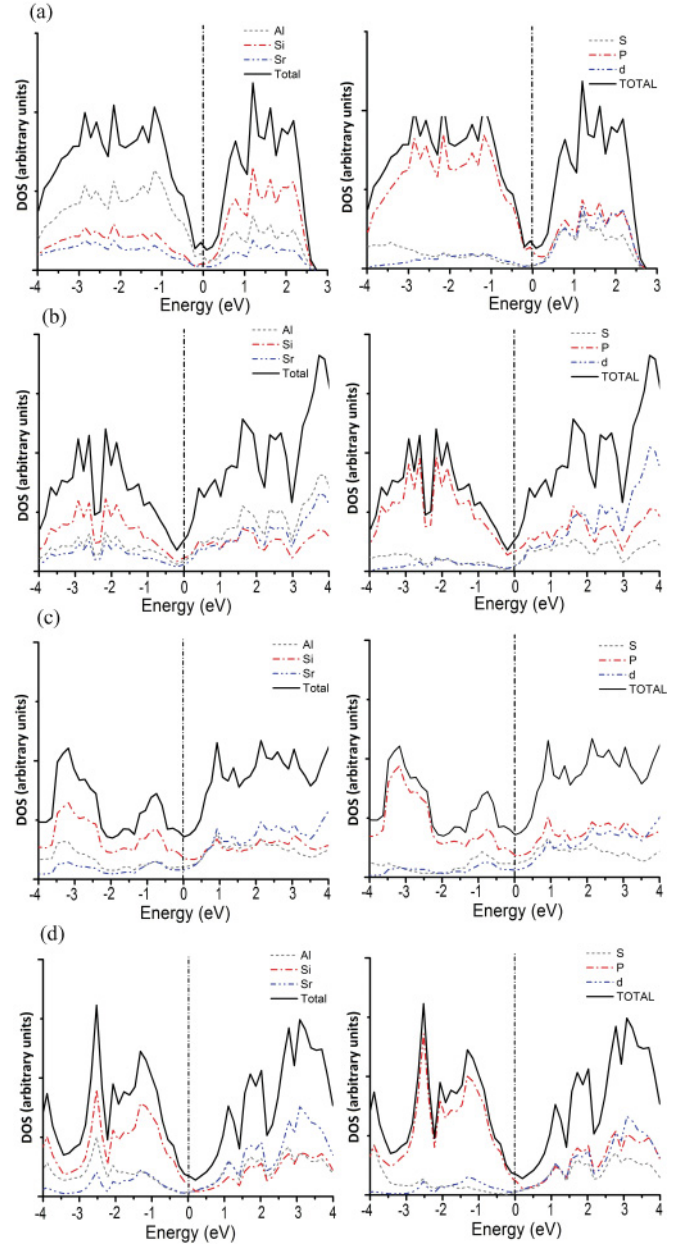


FIG. 2. (Color online) Partial and total density of states calculated by the LDA approximation. The DOS is given in normalized arbitrary units by taking as reference the trigonal phase. Panels correspond to (a) op20, (b) os20, (c) tI10, and (d) tri.

smaller for this structure than the previous cases. The Si-Si interactions in the os20 and tI10 phases are responsible for the increment of the  $p$  and  $s$  orbitals' contribution on the Fermi level. The maximum obtained by the Bader charge analysis<sup>32</sup> shows more delocalization between the Al-Si electrons in the tI10 phase, generating an increase of states close to the Fermi level and allowing the possibility of five coordination numbers for Si.

However, the electronic localization function (ELF) and the Bader analysis show that there are five atoms around the Si atoms, which are at the Si-Al distance 2.54 Å, and at the Si-Si distance 2.72 Å. The Al-Si atoms are completely bonded and

TABLE III. Charge average by atom calculated using Bader charge analysis.

Phase	Al	Si	Sr
op20	0.0000	7.6396	8.7208
os20	0.9068	6.7348	8.7168
tI10	0.0000	7.6027	8.7947
Tri	0.0000	7.6105	8.7790

the Si-Si atoms are weakly bonded. The analysis using the Zintl formalism is fulfilled for the tI10 phase, which is similar to the op20 and tri phases.

Table III shows the calculated charge by atom using the Bader analysis.<sup>32</sup> The aluminum atoms completely transfer their electrons, except for the os20 phase. The strontium atoms almost transfer their two electrons in order to have a closed valence shell. The incomplete charge transfer from Sr to Si is mainly due to the partial covalent character in the Sr-Si bonding.

The os20 phase differs from the op20 phase mainly from the Al-Al and Si-Si bonds, which are responsible for an increase in the number of the states at the Fermi level. In the case of the os20 phase, the Al-Al bonds are able to break the Zintl concept, because there is not a three-electron transfer from the aluminum atoms.

Figure 3 shows the ELF for the different phases along chosen high-symmetry planes. It shows that the first two structures are clathrates, which are formed by connecting Al-Si ribbons. The strontium atoms are transferring the charge to the silicon atoms between the different ribbons. The trigonal and the tI10 are layered phases; the trigonal phase, as shown in Fig. 3, shows perfect rearrangement of the Al-Si bonds, forming hexagonal rings, which are located between the Sr layers. In the case of the tI10 phase, there is the formation of Al-Si layers between the Sr atoms, with charge transfer between the silicon toward the Sr atoms, as shown in Fig. 3.

### C. Mechanical properties and stability

In this section, we discuss the elastic properties as calculated from a frozen approach to the stress tensor. The energy-volume data was fitted to a third-order Birch-Murnaghan equation,<sup>33,34</sup> where the bulk modulus  $B_0$  and its derivative  $B'_0$  can be extracted. The elastic constants were calculated following the expansion discussed in Sec. II B. Table IV summarizes the calculated elastic constants of the bulk modulus. Due to the absence of experimental information, we have used different exchange correlations (LDA, GGA-PW91, and GGA-AM05) to consider the overestimation and underestimation of those quantities, as already noted in volume-dependent properties. We notice that layered phases have a higher bulk modulus than clathrate phases, even though all obtained bulk moduli happen to be smaller than those obtained from pure aluminum

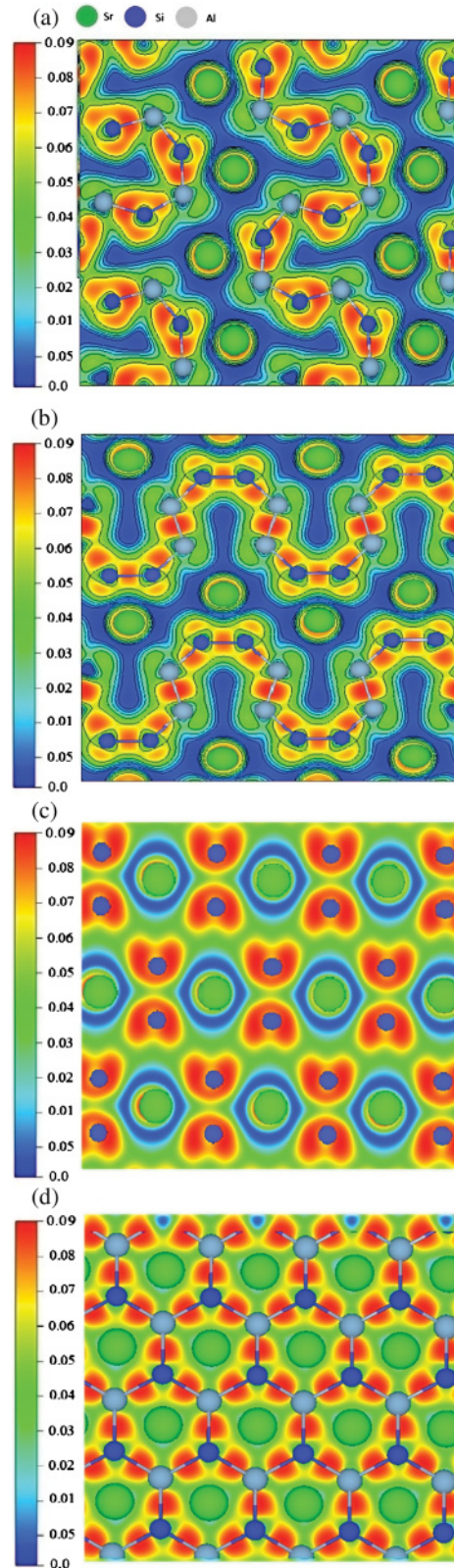


FIG. 3. (Color online) Electronic localization function (ELF) calculated for different planes: (a) op20 (010), (b) os20 (110), (c) tI10 (001), and (d) tri (001).

and silicon in their ground state. The Al-Si-Sr orthorhombic clathrates have a bulk modulus smaller than the silicon clathrates,<sup>35</sup> mainly due to the ionic character of the Si-Al bonds.

The requirements for mechanical stability in a trigonal, tetragonal, and orthorhombic structure are set from the following restrictions on the elastic constants.<sup>36</sup>

For the trigonal structure,

$$\begin{aligned} C_{11} > 0, \quad C_{44} > 0, \quad C_{11} - C_{12} > 0, \\ (C_{11} + C_{12})C_{33} - 2C_{13}^2 > 0. \end{aligned} \quad (4)$$

For the tetragonal structure,

$$\begin{aligned} C_{11} > 0, \quad C_{33} > 0, \quad C_{44} > 0, \quad C_{66} > 0, \\ C_{11} - C_{12} > 0, \quad C_{11} + C_{33} - 2C_{13} > 0, \\ (2C_{11} + C_{33} + 2C_{12} + 4C_{13}) > 0. \end{aligned} \quad (5)$$

For the orthorhombic structure,

$$\begin{aligned} C_{11} > 0, \quad C_{22} > 0, \quad C_{33} > 0, \\ C_{44} > 0, \quad C_{55} > 0, \quad C_{66} > 0, \\ (C_{11} + C_{22} - 2C_{12}) > 0, \\ (C_{11} + C_{33} - 2C_{13}) > 0, \\ (C_{22} + C_{33} - 2C_{23}) > 0, \\ (C_{11} + C_{22} + C_{33} + 2C_{12} + 2C_{13} + 2C_{23}) > 0. \end{aligned} \quad (6)$$

The elastic constants reported in Table IV satisfy the stability conditions for all exchange-correlation functionals. The  $C_{ij}$  with  $i = j$  are greater than zero and, on average, two times greater than the  $C_{ij}$  with  $i \neq j$ . For the case of the os20 phase, it is close to an instability because the  $C_{66}$  value for the LDA exchange correlation is negative, and for the GGA-PW91 and GGA-AM05, it is close to zero.

Figure 4 shows the stability of the phases as a function of volume, with the LDA, GGA-PW91, and GGA-AM05 exchange correlations. In order to fit the equation of state (EOS), a compression and an expansion of around 30% of the equilibrium volume in steps of 10% were used. Optimization of internal coordinates at each nonequilibrium volume was performed.

We also conclude that the elastic stability from Table II indicates that the trigonal structure happens to be the most stable amongst those considered here.

In order to determine the critical pressure, we employed the classical thermodynamic relation

$$\left( \frac{\partial E}{\partial V} \right)_s = -P. \quad (7)$$

Due to the fact that all calculations were performed at 0 K, it is possible to use Eq. (7), where the entropy is a constant. Therefore, the critical pressure is determined when the slopes of the  $E$ - $V$  curves are the same (equal enthalpy).

However, the use of different exchange correlations produces significant changes in the numerical values, even though the trends are similar. In the case of the LDA and GGA-AM05

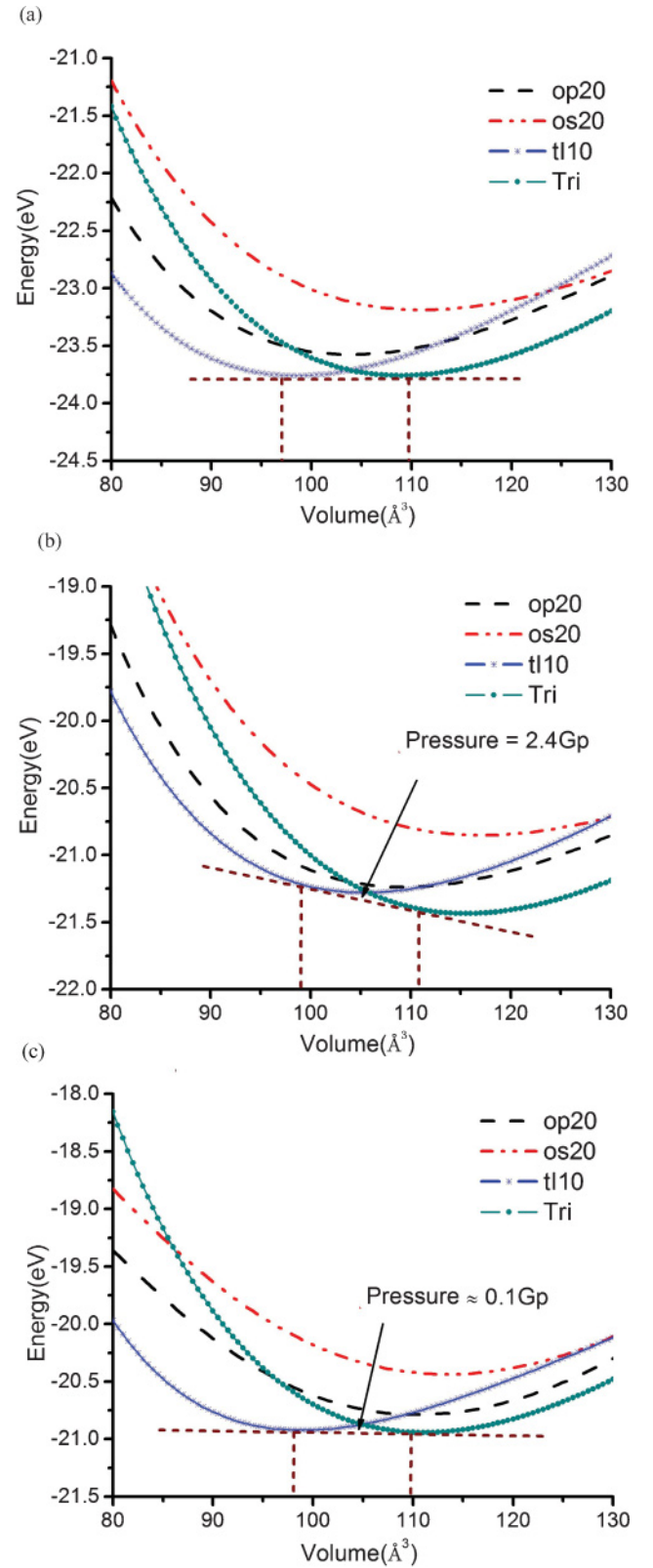


FIG. 4. (Color online) Calculated energy-volume curves for (a) LDA, (b) GGA-PW91, and (c) GGA-AM05. The energy was normalized according to the unit formula of the trigonal phase.

TABLE IV. Mechanical properties calculated (in GPa) by LDA, GGA-PW91, and GGA-AM05 approximations for the  $\text{Al}_2\text{Si}_2\text{Sr}$  phases.

Phase	$C_{11}$	$C_{22}$	$C_{33}$	$C_{12}$	$C_{13}$	$C_{23}$	$C_{44}$	$C_{55}$	$C_{66}$	$B_0$	$B'_0$
op20											
LDA	84.5	122.1	129.5	47.5	47.3	39.8	20.2	29.4	30.7	50	4.2
GGA-PW91	81.3	114.5	120.3	38.1	44.4	33.5	17.9	26.3	29.2	43.8	4.7
GGA-AM05	81.9	117.1	124.7	45.9	45.6	34.8	29.5	30.4	31.3	45.9	4.3
os20											
LDA	105	99.9	88.6	44.1	45.6	42.7	24	30.8	-3.7	43.3	3.8
GGA-PW91	97.4	95.1	85.9	39.4	39.2	39.1	22.7	32.4	2.07	36.9	4.3
GGA-AM05	101	100	88.2	44.1	47	42.7	22.6	34.7	4.48	44.4	4.1
tI10											
LDA	121	121	69.3	54	51.1	51.1	35.9	35.9	49.1	55.7	4.6
GGA-PW91	101	101	31.4	42	37.1	37.1	22.2	22.2	39.4	46.9	4.6
GGA-AM05	102	102	82.6	46	47	47	30.3	30.3	48.6	53.1	4.5
Tri											
LDA	134.7	134.7	104.2	46	33.4	33.4	38.6	38.6	44.3	59.1	3.9
GGA-PW91	110.3	110.3	72.5	23.5	49.1	49.1	11.4	11.4	43.4	52.6	3.8
GGA-AM05	128.2	128.2	102	42.2	30.1	30.1	35.6	35.6	43	60	3.8

calculations, the trigonal-tetragonal phase transition occurs around 0.1 GPa, while GGA-PW91 occurs at 2.4 GPa. The os20 and op20 phases are metastable phases, and the os20 phase curve has large enthalpy values, which somewhat correlates with the fact that this structure is at the limit of mechanical stability. In Fig. 4, we can see that in the absence of the tI10 phase, the trigonal-orthorhombic phase transition can occur at higher pressures. Therefore, the op20 phase is a metastable phase with a  $\Delta H^{\text{tri} \rightarrow \text{ort}} \approx 4.5$  kJ/(mol atom).

Under pressure, the op20 and trigonal phases show a small reduction in the Si-Al bond distance of around 10% from 0 to 75 GPa. A Bader charge analysis<sup>32</sup> shows that under compression, the electrons are more localized around the Si atoms and the charge contribution of the strontium to silicon is smaller.

Figure 5 shows a comparison between the electronic density of states at low-pressure and high-pressure states.

We now discuss the dependence of the electronic density of states as a function of pressure for the tI10 and op20 phases (the os20 phase is too high in energy to be considered). In the trigonal phase, there is an increase of states close to the Fermi level due to the contribution of  $p$  orbitals. The pressure causes the layers between the Sr atoms to become closer, which increases the Si-Sr-Si interactions. Therefore, more  $p$  orbitals are occupied. The case of the op20 phase is totally different since under pressure the Al atoms gets closer, which in turn results in some Si atoms having five Al atoms in the coordination shell. These results were confirmed by the maxima analysis on the electronic density obtained by the Bader charge analysis and the electronic localization function. Due to the increase in the coordination number on the silicon atoms, the occupation of  $s$  and  $p$  orbitals increases and the conduction is now larger.

For the tI10 phase, the change in the  $d$  orbitals is noticeable, while the change in the  $p$  orbitals can only be noted close to the Fermi level. The most important change is in the contribution coming from the  $s$  orbitals, which increases.

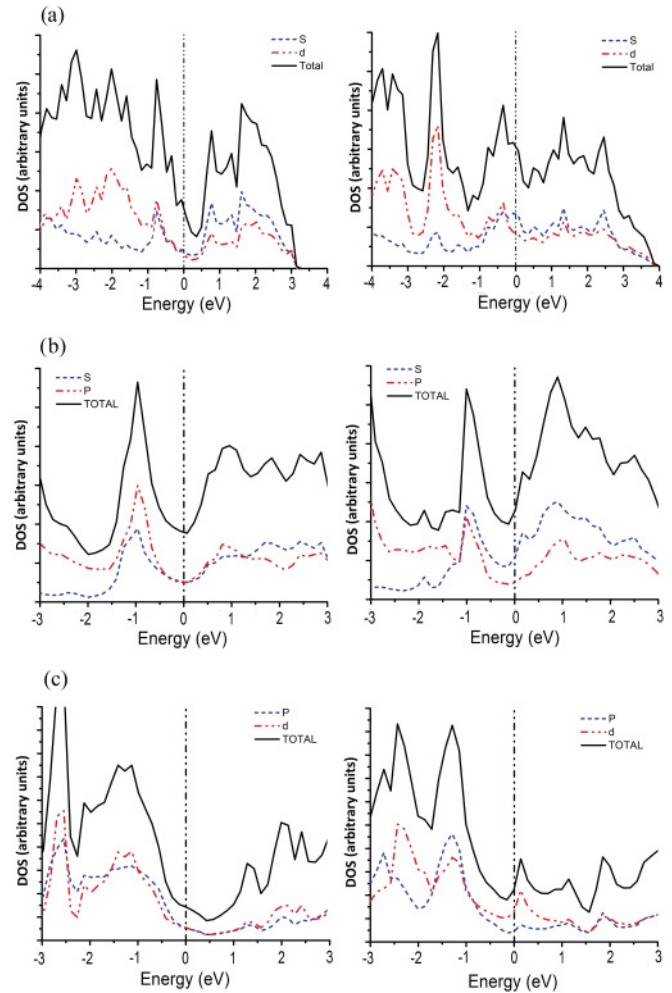


FIG. 5. (Color online) Calculated total and partial density of states at different pressure conditions for (a) op20, (b) tI10, and (c) trigonal phases. The left-hand side is at 13.5 GPa and the right-hand side is at 75 GPa.

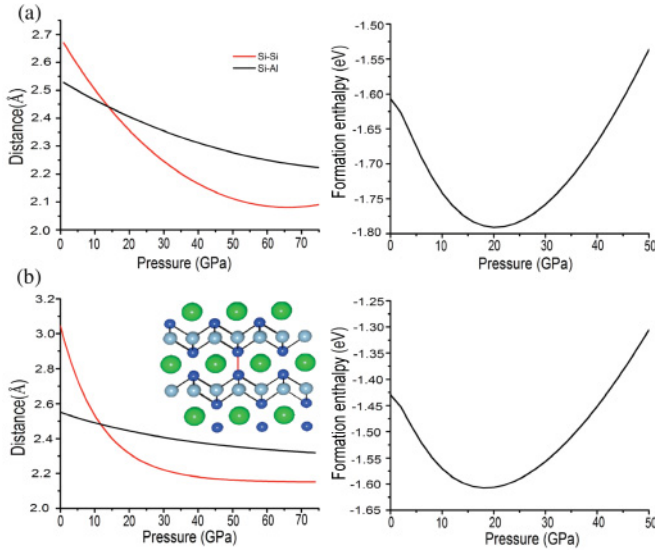


FIG. 6. (Color online) Comparison between Al-Si and Si-Si distances from 0 to 75 GPa and formation enthalpy for the tI10 phase for two different exchange correlations, (a) LDA and (b) GGA-PW91.

A possible explanation can be obtained by using the Bader charge analysis.<sup>32</sup> Basically, the electrons in the Al-Si bonds are less localized under pressure. Another important point for the stability of the tI10 phase at high pressures comes from the changes in the Al-Si and the Si-Si distance, which can be seen in Fig. 6.

The formation enthalpy was calculated according to the following equation:

$$\Delta H_f = E_{(P)}^{tI10} - 2 \times E_{(P)}^{Al} - 2 \times E_{(P)}^{Si} - E_{(P)}^{Sr}, \quad (8)$$

where  $E_{(P)}^{tI10}$  is the energy of the tI10 phase calculated at different pressure conditions.  $E_{(P)}^{Al}$ ,  $E_{(P)}^{Si}$ , and  $E_{(P)}^{Sr}$  are the energy of the pure elements calculated at different pressure conditions in their reference structures (fcc for Al and Sr, and diamond cubic for Si).

At low pressures, the Al-Si distance is usually larger than the Si-Si distance for all considered phases, but for the tI10 phase, there is a critical change around 15 GPa where the Si-Si distance decreases dramatically, while the Al-Si distance remains almost constant. The main consequence is an increment in the stability at high pressures, as seen in Fig. 6. For the LDA and GGA-PW91 exchange correlations, there is a minimum in the formation enthalpy of around 20 GPa, with a critical value for the Si-Si distance of around 2.2 Å. The minimum value of the formation enthalpy indicates that at 20 GPa, the structure is more stable when the Si-Si distance is close to the typical value of 2.33 Å. After 20 GPa, the formation enthalpy increases and the structure becomes less stable.

The electronic structure of the tI10 phase is more propitious in increasing the thermoelectric behavior of the  $Al_2Si_2Sr$  alloy, with a similar effect derived by increasing the pressure, which basically increases the number of states close to the Fermi level. Therefore, the trigonal-tI10 phase transition can be favorable in improving the thermoelectric properties and reducing the mechanical properties, which, at the same time,

can decrease the effect of microfracture in cast Al-Si alloys with strontium as a modifier.

#### D. Vibrational properties

The vibrational properties were calculated as described in Sec. II C. For the phonon dispersion calculations, a  $2 \times 2 \times 2$  periodic supercell was used to calculate the interatomic-force constants at specific symmetry points. Then, an interpolation technique was used to obtain values to other  $Q$  points.<sup>26</sup> For the studied phases, experimental information is not available, therefore the results validation was along the same lines as found in Ref. 37.

Figure 7 shows the phonon dispersion and its projected phonon density of states; the dashed line corresponds to the Debye frequency. No vibrational instability is observed from the results of the four considered phases. For the clathrate phases (os20 and op20), the low-frequency modes dominate. The low modes primarily correspond to Sr atoms inside Al-Si cages. The os20 structure has an increase in modes for aluminum atoms due to Al-Al bonding, in the same way that the modes for silicon atoms have increased at frequencies above the Debye frequency. The Al-Al and Si-Si bonds show an effect in the optical phonon modes at high frequencies where they remain almost constant, while in the op20 structure in which there are only Si-Al bonds, the high-optic branches are more scattered.

For the layered phases (trigonal and tI10), there is a well-defined peak ( $3 \times 12$  Hz) in the acoustic modes that corresponds to the strontium atoms. A second peak can be observed around  $4 \times 12$  Hz; this peak is the sum of the low-frequency optic modes. The three kinds of atoms contribute to the peak. Unlike the clathrate phases, in the layered phases there is a high contribution of the strontium to this peak. In the middle part of the phonon density of states, the trigonal phase has two peaks, one at  $7 \times 12$  Hz and the other at  $8.25 \times 12$  Hz, which correspond to the Al-Si rings. Compared to the tI10 phase, it is possible to observe a distortion in the frequencies cited above due to the fourfold Al-Si coordination. A large difference exists at high frequencies where, around  $1 \times 13$  Hz, there are at least two times as many modes in the layered phases as in the clathrate phases.

No band gaps were observed in any of the calculated phonon density of states, and the maximum frequency is not considerably larger than the Debye frequency. Therefore, the phases are Debye-like solids and the thermal behavior could be properly described by using the Debye model. As seen in Fig. 7, the Debye frequencies for all phases are rather close. However, the heat-capacity behavior is different at low temperatures. Figure 8 shows the characteristic behavior of the heat capacity, where for the clathrate phases, the high density of states at low frequencies (0 and  $6 \times 12$  Hz) and the strong contribution of the TA phonon modes is noticed in the increment of the  $C_v/T^3$  maximum with respect to the layered phases. The interpretation of the heat capacity on the  $T^3$  normalization is based on the expected contribution of the phonons at low temperature; deviations are shown as the linear increase in this figure. A similar interpretation, but for different compounds, was discussed in Ref. 38.

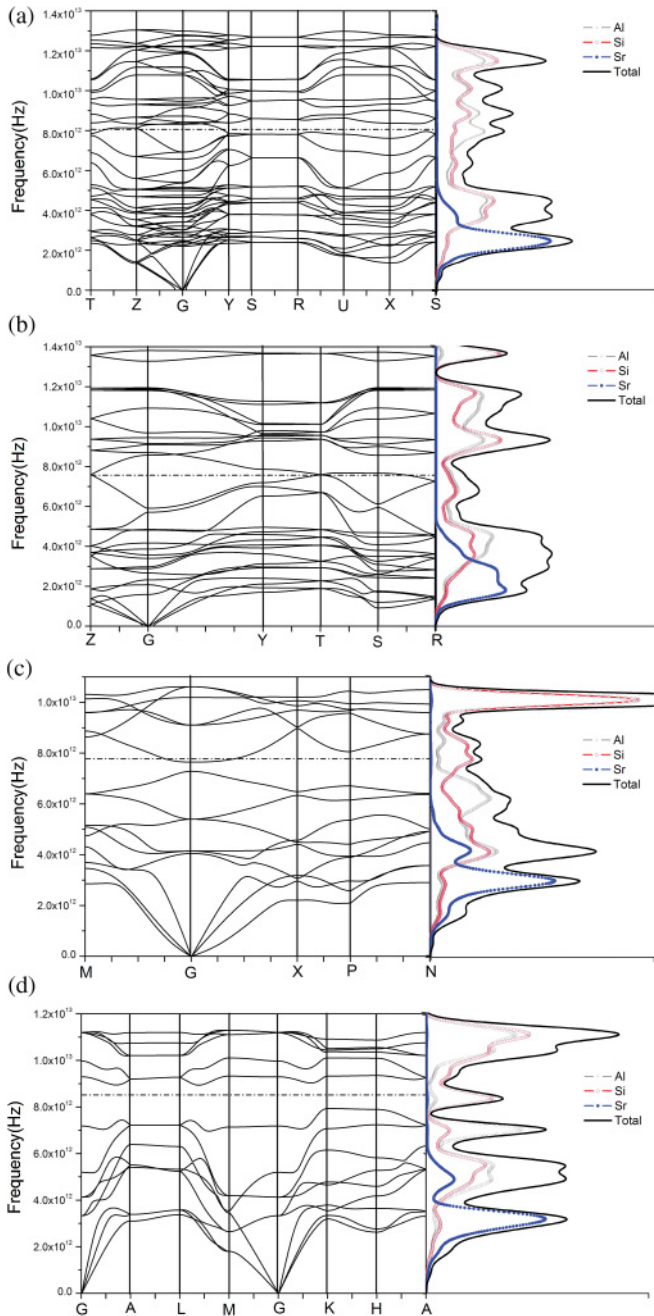


FIG. 7. (Color online) Phonon dispersion curves in the major symmetric directions and phonon density of states.

For the trigonal and tI10 phases, there is a double peak in the  $C_v/T^3$  maximum, which correlates to different contributions to the  $C_v$  growth from different phonon branches. It is clearer in the tI10 phase, where there is a peak at 5 K and another at 25 K; this effect is due to the softening of the LA phonon modes. An important difference in the behavior of the heat capacity between the trigonal and tI10 phases was found, where for the tI10 phase, the optic modes are less scattered. Therefore,

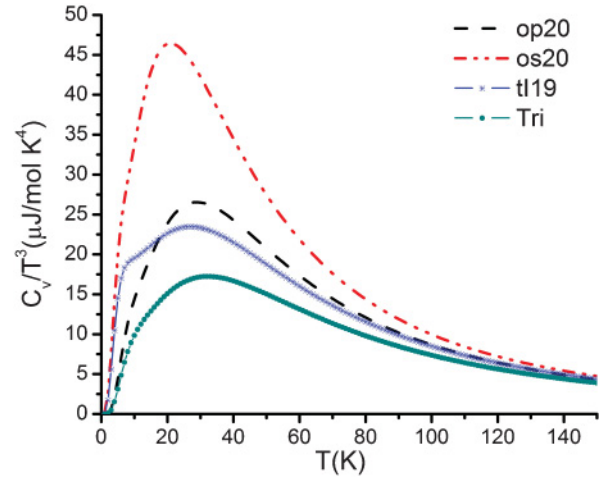


FIG. 8. (Color online) Temperature dependence of  $C_v/T^3$  in the  $T$  region from 0 to 150 K.

the tI10 phase has a larger heat capacity than the trigonal phase.

Figure 10 shows the free-energy–temperature curves calculated with the LDA, GGA-PW91, and GGA-AM05 exchange–correlation functionals. In the LDA approximation, the phase transition occurs around 650 K, while for the os20 and op20, the temperature does not have an important effect on the stability. The GGA-PW91 and GGA-AM05 approximations do not show any phase transition, the op20 phase is more stable than the tI10 phase at high temperatures in the GGA-PW91 approximation while in GGA-AM05 the tI10 is more stable than the op20 phase. For the os20 phase, the result is the same as in the LDA calculations, with the energy difference with respect to the trigonal phases being larger.

The free energy between the trigonal and tI10 phases is very close at high temperatures with the LDA and GGA-AM05 exchange–correlation functionals; the LDA calculations show a phase-transition temperature. The pressure effect on the phase transition can be known if we now treat the thermal expansion

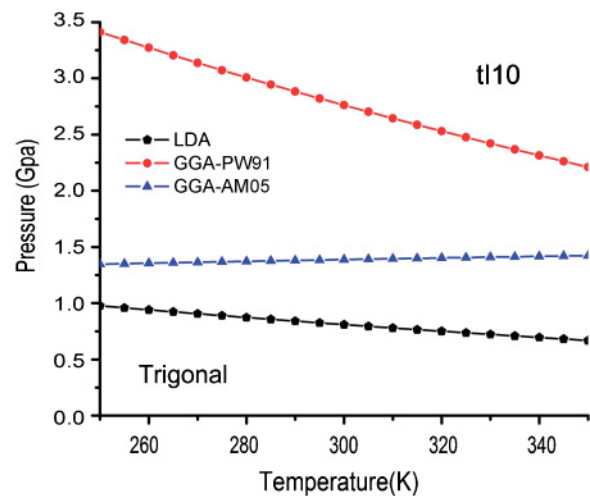


FIG. 9. (Color online) Temperature–pressure dependence of the phase transition between the trigonal and tI10 phases.

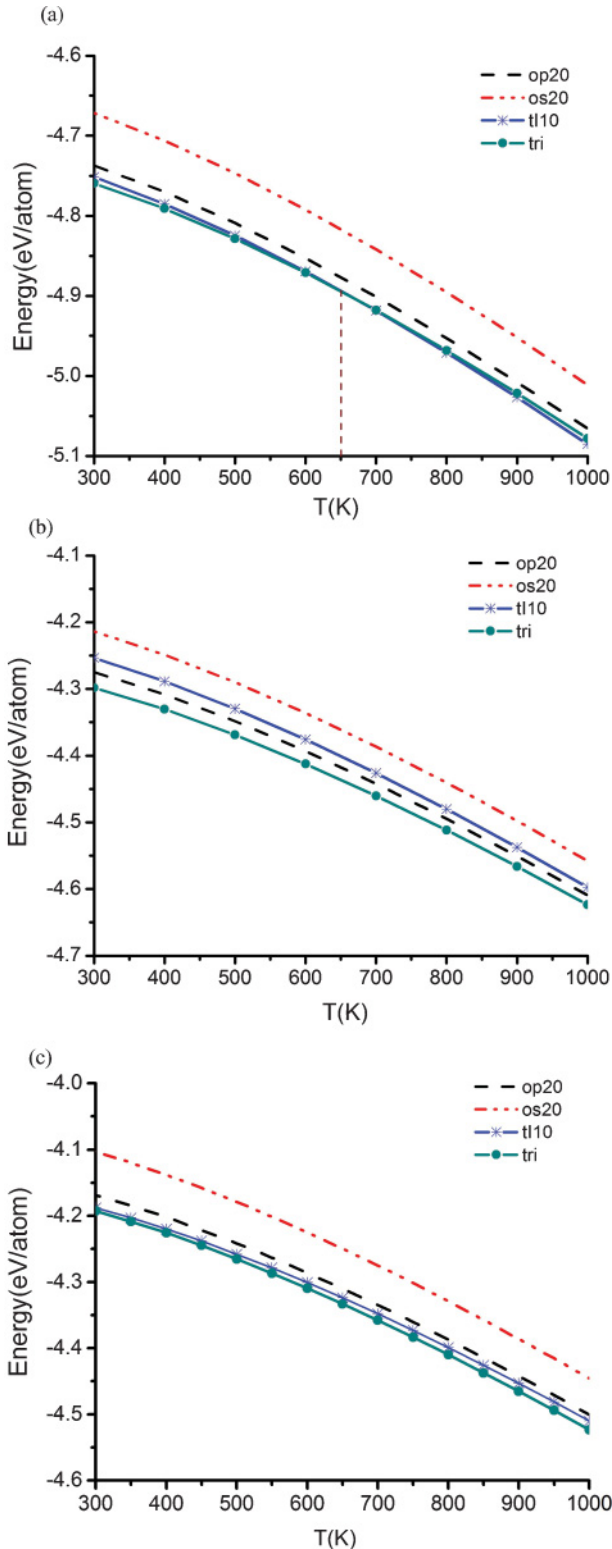


FIG. 10. (Color online) Energy-temperature curves calculated according to Eq. (3). The energy is normalized by atom. (a) LDA, (b) GGA-PW91, and (c) GGA-AM05.

as a function of the temperature. However, that is outside the scope of this paper. An easy way to find the equilibrium line between two phases and the temperature-pressure relation is

by using the Clausius-Clapeyron equation,

$$P = P^* + \left( \frac{\Delta H}{\Delta V} \right) \ln \left( \frac{T}{T^*} \right). \quad (9)$$

The  $P^*$  and  $T^*$  are the pressure and the temperature of reference, and the  $\Delta H$  and  $\Delta V$  are the change in the enthalpy and volume, respectively. The Clausius-Clapeyron equation is valid only in a short range, where it is possible to consider that the volume varies linearly. Figure 9 shows the variation of the pressure transition by temperature; the calculations were done assuming that there is a temperature transition at 650 K, and 0 Gp is the reference pressure.

For the LDA and GGA-PW91 approximations, we can see that the pressure decreases as expected. The case of GGA-AM05 is different because the  $\Delta H/\Delta V$  slope is near zero and positive, hence the transition pressure remains almost constant.

According to the recent work of Kauzlarich,<sup>4</sup> there is a small endotherm at about 550 °C in the thermal gravimetry and differential scanning calorimetry (TG-DSC) measurements that was not completely identified. The endotherm was attributed to a small amount of Al-Si eutectic. From Fig. 10 and the small energy difference between the trigonal and tI10 phases, the endotherm may be attributed to the trigonal-tetragonal phase transition in the  $\text{Al}_2\text{Si}_2\text{Sr}$  phase, although this assertion clearly requires experimental verification.

#### IV. CONCLUSIONS

In the present work, the mechanical, electronic, vibrational, and thermodynamic properties of the  $P\bar{3}m1$ ,  $I4/mmm$ ,  $Cmcm$ , and  $Pnma$  crystal structures with the  $\text{Al}_{0.4}\text{Si}_{0.4}\text{Sr}_{0.2}$  composition have been investigated using DFT calculations within the LDA, GGA-PW91, and GGA-AM05 exchange correlations. The electronic structure of the trigonal, tI10, and op20 phases suggest that these crystal structures can be described as Zintl phases. In the case of the os20 phase, the Zintl concept is incomplete, mainly due to the Al-Al bonds where, according to the Bader analysis, the charge transfer is incomplete from the Al atoms to Si atoms. The os20 and the tI10 phases have larger participation of  $p$  orbitals in the Fermi level due to the Si-Si bonding. In particular, for these phases, the presence of the  $p$  orbitals increases the metallic behavior.

The energetic and mechanical stability has been studied and it was determined that the four phases are energetic and mechanically stable. The ground-state phase is the trigonal phase, but the energetic difference between the trigonal and tI10 phases is very small. The mechanical properties for the four crystal structures were determined to be low compared to the mechanical properties of the pure elements (Al, Si).

The pressure effects were studied and the tI10 phase was found to be more stable under high-pressure conditions. For the tI10 phase, 20 GPa is the critical value for the stability. The Si-Al distance does not significantly change as the pressure increases, however, the Si-Si distance provides an important contribution to the stability of the phases at high pressure, mainly for the tI10 phase. The electronic density of states is altered by the very-high-pressure conditions, increasing the number of states at the Fermi level for the trigonal and op20 phases.

The vibrational properties were also determined, where no negative frequencies were observed and the thermal behavior can be summarized in line with the Debye model. The Debye frequencies were calculated and small differences were found between the different phases. Therefore, the heat capacity happens to be very close between each phase. The free-energy–temperature curves of all the structures were calculated for the LDA, GGA-PW91, and GGA-AM05 exchange correlations. In the LDA approximation, there is a trigonal–tetragonal phase transition around 650 K. For the GGA-PW91 approximation, the trigonal phase is always more stable than the tI10 phase, and the phase transition is not clear. However, the GGA-AM05 approximation showed that the tI10 phase is stable even at low temperatures. The increase of the density of states at the Fermi level and the increase of the heat capacity of the tI10 phase show that this phase can have significant thermoelectric properties; the temperature–pressure and energy–volume curves show that it is possible to stabilize the tI10 at low temperatures.

In summary, the trigonal–tetragonal phase transition can exist under certain pressure and temperature conditions, and the tI10 phase is favorable for use as a thermoelectric material. The

op20 phase is a clathrate metastable phase, with  $\Delta H^{\text{tri} \rightarrow \text{ort}} \approx 4.5$  kJ/(mol atom). The os20 phase is a metastable phase with a large energy difference compared to the ground state.

#### ACKNOWLEDGMENTS

The authors would like to acknowledge the TAMU-CONACyT program for its support. A.H.R. would like to acknowledge the support of CONACyT under Project No. J-83247-F and FNRS-CONACyT Bi-national Collaboration. G.T.A. acknowledges CONACyT (México) for its support through Grant No. 216341. First-principles calculations were carried out in the Chemical Engineering Cluster and the Super-Computer Facility of Texas A&M University as well as the Texas Advanced Computing Center. R.A. also acknowledges partial support from Grants No. NSF-DMR-0805293 and CMMI-1027689. Preparation of the input files for the electronic-structure calculations and analysis of the data have been performed within the framework AFLOW/ACONVASP [39] developed by Stefano Curtarolo as well as with the ATAT package<sup>28,40</sup> developed by Axel van de Walle.

- 
- <sup>1</sup>J. E. Gruzleski and B. M. Closset, *The Treatment of Liquid Aluminum-Silicon Alloys* (American Foundrymen's Society, Des Plaines, IL, 1990).
- <sup>2</sup>I. N. Ganiyev, A. V. Vakhobov, T. D. Dzhurayev, and F. N. Alidzhanov, *Dokl. Akad. Nauk Tadzh. SSR* **19**, 51 (1976).
- <sup>3</sup>S. Lu and A. Hellawell, *Metall. Mater. Trans. A* **18**, 1721 (1987).
- <sup>4</sup>S. Kauzlarich, C. Condrón, J. Wassei, T. Ikeda, and G. Snyder, *J. Solid State Chem.* **182**, 240 (2009).
- <sup>5</sup>B. B. Iversen, A. E. C. Palmqvist, D. E. Cox, G. S. Nolas, G. D. Stucky, N. P. Blake, and H. Metiu, *J. Solid State Chem.* **149**, 455 (2000).
- <sup>6</sup>H. Shimizu, T. Kume, Y. Narita, S. Sasaki, T. Kikudome, and S. Yamanaka, *Phys. Status Solidi B* **244**, 357 (2007).
- <sup>7</sup>H. Shimizu, T. Kume, Y. Narita, S. Sasaki, T. Kikudome, and S. Yamanaka, *Phys. Status Solidi B* **244**, 357 (2007).
- <sup>8</sup>S. Yamanaka, M. Kajiyama, S. Sivakumar, and H. Fukuoka, *High Press. Res.* **24**, 481 (2004).
- <sup>9</sup>Z. Ban and M. Sikić, *Acta Crystallogr.* **18**, 594 (1965).
- <sup>10</sup>C. Zheng, R. Hoffmann, R. Nesper, and von Schnering, *J. Am. Chem. Soc.* **108**, 1876 (1986).
- <sup>11</sup>J. Iglesias, K. E. Pachali, and H. Steinfink, *J. Solid State Chem.* **9**, 6 (1974).
- <sup>12</sup>J. Iglesias and H. Steinfink, *Z. Kristallogr.* **142**, 398 (1975).
- <sup>13</sup>W. Kohn and L. Sham, *Phys. Rev.* **140**, A1133 (1965).
- <sup>14</sup>G. Kresse and J. Furthmüller, *Phys. Rev. B* **54**, 11169 (1996).
- <sup>15</sup>G. Kresse and J. Furthmüller, *Comput. Mater. Sci.* **6**, 15 (1996).
- <sup>16</sup>J. Perdew and A. Zunger, *Phys. Rev. B* **23**, 5048 (1981).
- <sup>17</sup>J. Perdew and Y. Wang, *Phys. Rev. B* **45**, 13244 (1992).
- <sup>18</sup>R. Armiento and A. E. Mattsson, *Phys. Rev. B* **72**, 085108 (2005).
- <sup>19</sup>A. E. Mattsson, R. Armiento, J. Paier, G. Kresse, J. M. Willis, and T. R. Mattsson, *J. Chem. Phys.* **128**, 084714 (2008).
- <sup>20</sup>H. J. Monkhorst and J. D. Pack, *Phys. Rev. B* **13**, 5188 (1976).
- <sup>21</sup>M. Methfessel and A. Paxton, *Phys. Rev. B* **40**, 3616 (1989).
- <sup>22</sup>P. Blöchl, O. Jepsen, and O. Andersen, *Phys. Rev. B* **49**, 16223 (1994).
- <sup>23</sup>H. Guo, X. Chen, J. Zhu, L. Cai, and J. Gao, *Chin. Phys. Lett.* **22**, 1764 (2005).
- <sup>24</sup>L. Fast, J. M. Willis, B. Johansson, and O. Eriksson, *Phys. Rev. B* **51**, 17431 (1995).
- <sup>25</sup>O. Beckstein, J. Klepeis, G. Hart, and O. Pankratov, *Phys. Rev. B* **63**, 134112 (2001).
- <sup>26</sup>A. van de Walle and G. Ceder, *Rev. Mod. Phys.* **74**, 11 (2002).
- <sup>27</sup>S. Wei and M. Chou, *Phys. Rev. Lett.* **69**, 2799 (1992).
- <sup>28</sup>A. van de Walle, M. Asta, and G. Ceder, *CALPHAD* **26**, 539 (2002).
- <sup>29</sup>I. N. Ganiyev, A. V. Vakhobov, and T. D. Dzhurayev, *Russ. Metall.* **4**, 175 (1977).
- <sup>30</sup>N. Blake, D. Bryan, S. Lattner, L. Møllnitz, G. Stucky, and H. Metiu, *J. Chem. Phys.* **114**, 10063 (2001).
- <sup>31</sup>R. Nesper, *Prog. Solid State Chem.* **20**, 1 (1990).
- <sup>32</sup>W. Tang, E. Sanville, and G. Henkelman, *J. Phys. Condens. Matter* **21**, 084204 (2009).
- <sup>33</sup>F. D. Murnaghan, *Proc. Natl. Acad. Sci. USA* **30**, 244 (1944).
- <sup>34</sup>F. Birch, *J. Geophys. Res.* **57**, 227 (1952).
- <sup>35</sup>A. San-Miguel and P. Toulemonde, *High Press. Res.* **25**, 159 (2005).
- <sup>36</sup>D. Wallace and H. Callen, *Thermodynamics of Crystals* (Dover, New York, 1998).
- <sup>37</sup>A. Garay, M. Williams, G. Trapaga, and R. Arroyave, *J. Alloys Compd.* **484**, 822 (2009).
- <sup>38</sup>M. Cardona, R. K. Kremer, R. Lauck, G. Siegle, A. Muñoz, A. H. Romero, and A. Schindler, *Phys. Rev. B* **81**, 075207 (2010).
- <sup>39</sup>W. Setyawan and S. Curtarolo, *Comp. Mater. Sci.* **49**, 299 (2010).
- <sup>40</sup>A. van de Walle, *CALPHAD* **33**, 266 (2009).